Article:

Gomez Martin, JC, Gálvez, O, Baeza-Romero, MT et al. (3 more authors) (2013) On the mechanism of iodine oxide particle formation. Physical Chemistry Chemical Physics, 15 (37). 15612 - 15622. ISSN 1463-9076

https://doi.org/10.1039/c3cp51217g

View Article Online
View Journal

PCCP

Accepted Manuscript

This article can be cited before page numbers have been issued, to do this please use: J. C. Gomez Martin, Ó. Gálvez, M. T. B. Romero, T. Ingham, J. M. C. Plane and M. A. Blitz, *Phys. Chem. Chem. Phys.*, 2013, DOI: 10.1039/C3CP51217G.

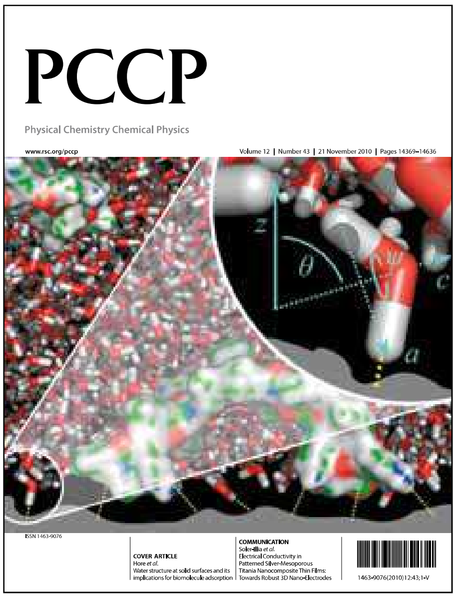

This is an *Accepted Manuscript*, which has been through the RSC Publishing peer review process and has been accepted for publication.

Accepted Manuscripts are published online shortly after acceptance, which is prior to technical editing, formatting and proof reading. This free service from RSC Publishing allows authors to make their results available to the community, in citable form, before publication of the edited article. This *Accepted Manuscript* will be replaced by the edited and formatted *Advance Article* as soon as this is available.

To cite this manuscript please use its permanent Digital Object Identifier (DOI®), which is identical for all formats of publication.

More information about *Accepted Manuscripts* can be found in the **Information for Authors**.

Please note that technical editing may introduce minor changes to the text and/or graphics contained in the manuscript submitted by the author(s) which may alter content, and that the standard **Terms & Conditions** and the **ethical guidelines** that apply to the journal are still applicable. In no event shall the RSC be held responsible for any errors or omissions in these *Accepted Manuscript* manuscripts or any consequences arising from the use of any information contained in them.

RSC Publishing

www.rsc.org/pccp
Registered Charity Number 207890

Abstract

View Article Online
DOI: 10.1039/C3CP51217G

The formation of atmospherically relevant iodine oxides I_xO_y (x = 1,...,3, y = 1,...,7) has been studied experimentally using time-of-flight mass spectrometry combined with a soft ionisation source, complemented with ab initio electronic structure calculations of ionisation potentials and bond energies at a high level of theory presented in detail in the accompanying paper (Galvez, *et al.*, 2013). For the first time, direct experimental evidence of the I_2O_y (y = 1,...,5) molecules in the gas phase has been obtained. These chemical species are observed alongside their precursors (IO and OIO) in experiments where large amounts of aerosol are also generated. The measured relative concentrations of the I_xO_y molecules and their dependence on ozone concentration have been investigated by using chemical modelling and rate theory calculations. It is concluded that I_2O_4 is the most plausible candidate to initiate nucleation, while the contribution of I_2O_5 in the initial steps is likely to be marginal. The absence of large I_3O_y (y = 3,...,6) peaks in the mass spectra and the high stability of the I_2O_4-I_2O_4 dimer indicate that dimerisation of I_2O_4 is the key step in iodine oxide particle nucleation.

1. Introduction

Iodine oxides are ubiquitous in the marine and polar boundary layer,[1-5] where they form by ozone-driven photo-oxidation of iodocarbons and molecular iodine emitted from the sea or ice as a result of biotic and abiotic processes (see Saiz-Lopez et al.[6] and references therein):

I_2, CH_3I, CH_2I_2, etc. + hν → I + products (R1)

$I + O_3 \rightarrow IO + O_2$ (R2)

From early laboratory studies on gas-phase iodine chemistry it is well known that the recombination of iodine monoxide (IO) precedes the formation of condensable chemical species, which can undergo nucleation and lead to the formation of optically detectable aerosol and solid deposition.[7-10] In fact, it has been shown that emission fluxes of molecular iodine from coastal macroalgae under oxidative stress at low tide are strong enough to sustain substantial secondary aerosol formation in the atmosphere.[11-13] This potential link between marine biota and a climatically sensitive variable such as the aerosol loading, besides photosensitized iodine-driven ozone depletion, has motivated numerous laboratory field studies in recent years.[6]

A number of theoretical and experimental studies have tried to rationalise the formation mechanism of iodine oxide particles (IOPs). The key gas phase precursor of IOPs is iodine dioxide, formed from the IO self reaction with a 40% branching ratio at 1 atm in N_2:[14, 15]

$IO + IO \rightarrow OIO + I$ (R3a)

$IO + IO + M \rightarrow IOIO + M$ (R3b)

Based on the heat of formation of OIO and RRKM calculations, the lifetime of IOIO against thermal decomposition at 1 Atm and 293 K has been estimated to be ~ 1 s.[16] Also, tentative

View Article Online
DOI: 10.1039/C3CP51217G

assignments of the UV-vis spectrum of IOIO and estimates of its absorption cross sections yield atmospheric lifetimes of tens of seconds.[14, 15] Therefore, it has been commonly assumed[17] that R3 proceeds effectively through R3a under boundary layer conditions, and that the following step of the particle formation mechanism involves only OIO. The photo-instability of this species[18] will on the other hand slow down the nucleation process.

Indirect evidence of IO and OIO recombination has been reported and rate coefficients of the order of 1×10^{-10} cm^3 $molecule^{-1}$ s^{-1} at 400 Torr have been estimated:[15]

$$IO + OIO + M \rightarrow I_2O_3 + M \qquad (R4)$$

$$OIO + OIO + M \rightarrow I_2O_4 + M \qquad (R5)$$

However, unambiguous spectroscopic evidence of I_2O_3, I_2O_4 or other I_xO_y species has not been published. In fact, it has been the lack of experimental techniques able to discriminate between different iodine oxides in the gas phase[14, 15, 18] that has hindered clear progress in understanding this gas-to-particle conversion mechanism. Instead, a number of studies have focused on inferring mechanistic information from the physical and chemical properties of IOPs using ultrafine condensation particle counters, nano-differential mobility analysers, transmission electron microscopy, and quantitative x-ray analysis,[19-23] and from the bulk properties[24, 25] of the known stable solid phase iodine oxides (I_2O_4, I_2O_5, I_4O_9).[26]

Initially, the chemical composition of the particles was suggested to be I_2O_4, based on the observed lack of hygroscopic growth of IOPs.[20] This led to the proposal of a mechanism where OIO was the nucleating monomer:

$$OIO + (OIO)_n \rightarrow (OIO)_{n+1} \qquad (R6)$$

View Article Online
DOI: 10.1039/C3CP51217G

A semi-quantitative description of laboratory observed particle number densities and size distributions, based on the homogeneous nucleation of gas phase OIO (R6), was proposed.[19, 22] However, subsequent studies reported a stochiometric ratio I:O of ~2.5, indicating that the composition of the particles was more likely I_2O_5.[21] It was then proposed that I_2O_5 could be the nucleating monomer, especially in view of its large calculated dipole moment.[27] A gas phase scheme based on oxidation steps for generation of I_2O_5 was proposed:

$$I_2O_2 \xrightarrow{O_3} I_2O_3 \xrightarrow{O_3} I_2O_4 \xrightarrow{O_3} I_2O_5 \qquad \text{(R7-R9)}$$

$$I_2O_5 + (I_2O_5)_n \rightarrow (I_2O_5)_{n+1} \qquad \text{(R10)}$$

where I_2O_2, I_2O_3 and I_2O_4 would also form from reactions 3-5. Saunders and Plane[21] found that the rate coefficient of the oxidation steps R7-9 would need to be faster than 6×10^{-13} molecule^{-1} cm^{-3} s^{-1} to enable gas phase I_2O_5 to form faster than iodine oxides of lower O/I ratio under their experimental conditions.

However, it has been recently shown that the presence of O_3 is not necessary to form particles, even though the final composition of IOPs is still I_2O_5.[23] It has been suggested[23] that such composition would then appear to result from re-structuring in the solid phase:

$$5\ I_2O_4 \rightarrow 4\ I_2O_5 + I_2 \qquad \text{(R11)}$$

However, the thermally induced decomposition of I_2O_5 occurs at 460 K.[28, 29] Electronic structure calculations have been published indicating stable I_4O_7 and I_4O_8 molecules.[23] This suggests that I_2O_3 and I_2O_4 formed in R4 and R5 would be the nucleating species rather than I_2O_5. Interestingly, increasing temperatures have an inhibiting effect on IOP formation, with the high negative activation energy observed (-78 kJ mol^{-1}) possibly reflecting the thermal decomposition of various iodine oxide aggregates.[23] According to the latest findings,[23] the

View Article Online
DOI: 10.1039/C3CP51217G

lack of hygroscopic growth of I_2O_5 particles[20] (bulk I_2O_5 is hygroscopic) would not be related to the chemical composition of the particles, but indicate that the adsorption of water onto the surface of the fractal-like IOP agglomerates leads to their collapse to form higher density particles, though of similar aerodynamic mobility.

In summary, even though valuable mechanistic information has been obtained by the analysis of IOP distribution properties under different chemical and physical conditions, the lack of direct qualitative and quantitative evidence about the precise mechanism persists. In fact, the IOP formation process in laboratory experiments has never been completely understood, with IOPs nucleating more slowly than expected - even under dry, room temperature conditions - but then growing faster than can be modelled using the current understanding of IOP formation described above (A. Mahajan and R. Saunders, personal communication).

In this paper we present a first experimental attempt to solve this problem by observing directly the formation of iodine oxides using photo-ionisation time of flight mass spectrometry (PI-TOF-MS)[30] coupled to a high pressure flow tube. Additionally, high level *ab initio* quantum calculations described in detail the accompanying paper[31] and master equation modelling are used synergistically to interpret the experimental results and gain new insights into the nucleation of IOPs.

2. Experimental

Preliminary experiments were performed at low-pressure (~ 1 Torr) where ground state atomic oxygen $O(^3P)$, generated via either 248 nm excimer laser photolysis of O_3 or microwave discharge of O_2, was reacted with I_2 to generate iodine oxides, which were sampled via a pinhole located in the wall of the flow tube.[30] These experiments failed to detect any oxides except IO, presumably due to wall losses, which is potentially a severe

View Article Online
DOI: 10.1039/C3CP51217G

problem with this off-axis sampling configuration. Consequently, the experiment was re-configured so that the gas was sampled on-axis and at higher pressures (~ 100 Torr) in order to reduce the influence of wall losses, where the reagents flow down the entire length of the flow tube before being sampled into the mass spectrometer via a pinhole.

For the on axis configuration, iodine oxides were generated by the slow dark reaction between I_2 and O_3,[26] where O_3 (~1% in O_2) was directly introduced into the flow tube (internal diameter = 1.0 cm, length = 70 cm), and mixed with He, which first passed through a trap containing I_2 crystals and then a mixing manifold before entering the flow tube. The O_3 concentration was determined in separate experiments where the flow was directed into an O_3 optical absorption detector and the concentration of gas-phase I_2 was estimated by assuming its equilibrium vapour pressure. Typical concentrations in these experiments were $[I_2] \sim 4 \times 10^{15}$ molecule cm^{-3} and $[O_3]$ was varied over the range from 5×10^{14} to 2×10^{16} molecule cm^{-3}. A 100 μm pinhole coupling the flow tube to the mass spectrometer was employed, enabling a range of pressures between 40 and 200 Torr, where moderate wall losses and significant iodine oxide formation allowed detection of these species, while at the same time limiting aerosol generation. This was found to be important for enabling reproducible experiments to be carried out without immediately blocking the pinhole. The contact time is determined by assuming diffusion-enabled plug flow regime ($R_e \sim 0.5$, $P_e \sim 7$, $D_a \sim 0.001$).[32, 33]

The PI-TOF-MS system used in this study has been described in detail elsewhere.[30] Species entering the mass spectrometer are ionized ~ 5 cm from the pinhole by 118 nm VUV light, produced by frequency-tripling in Xe the 355 nm output from a YAG laser. Following photo-ionization the ions are extracted and accelerated into the field-free flight region, before being reflected onto an electron multiplier to produce a mass spectrum in analogue or in ion

DOI: 10.1039/C3CP51217G

counting mode (Fig. 1a). While the counting mode is sensitive to small signals (iodine oxides), the analogue mode allows observation of large signals (e.g. I_2).[34] The mass resolution of the TOF-MS is better than 1 in 100 Da. It is therefore possible to resolve small clusters up to ~1200 Da with sufficient resolution to determine, e.g., whether I_2O_4 or I_2O_5 is the condensable unit of IOPs. Mass to charge calibration (Fig. 1b) is accurate to within 1 mass at m/z 127 and 2 mass units at m/z 493 (1σ).

Quantum chemistry calculations were carried out to estimate the ionisation potentials (IPs) of the I_xO_y species (Table 1). Geometries of neutral species were first optimised at MP2 level using for the iodine atom a 46 electron shape-consistent averaged relativistic effective potential (AREP)[35, 36] combined with a valence-only aug-cc-pVTZ (aVTZ) basis set;[37] for oxygen, a conventional, all-electron aVTZ basis sets was used. Subsequent CCSD(T) single point calculations were performed on the neutral optimised geometries, both for the neutrals and the cations, in order to calculate the vertical ionisation energies. A full description of these theoretical studies is provided in an accompanying paper.[31] The calculated IPs shown in Table 1 are in the range from 8.6 to 11.4 eV, corresponding to photons of 144.3 – 108.8 nm, i.e. close to but generally below the photo-ionisation energy employed in the experiments (10.5 eV, corresponding to a photon of 118 nm).

3. **Results**

Examples of TOF spectra acquired in ion-counting mode at two different contact times (calculated from pressure and flow rates) are shown in Fig 2. Taking the ratio between the IO peak (m/z 143) and the I_2O_4 peak (m/z 318) as a reference, the experiments at short contact time show a higher concentration of I_xO_y species relative to the IO precursor. Fig. 3 shows integrated peak signals for the major peaks present in the spectra of Fig. 1 from a typical sequence of experiments. Initially [O_3] was varied in a controlled manner but the progressive

View Article Online
DOI: 10.1039/C3CP51217G

blocking of the pinhole by aerosol caused the pressure to increase (Fig. 3a), eventually stopping the experiment until the pinhole was cleaned and the system re-evacuated. The most prominent signals all change in a similar manner with pressure and $[O_3]$ (Fig. 3c and Fig. 4), and are positively and significantly correlated to IO. Another group of weak peaks (Fig. 3d, mostly I_3O_y) are apparently reacting to the pressure cycle in the flow tube (anticorrelated to pressure) or are almost flat, as shown by their absence from the difference between high and low ozone spectra (Fig. 1b and 1d). Mass signals not showing a dependence on O_3 (Fig. 3d) are interpreted as fragments of solid iodine oxide formed on the walls or the pinhole itself. In fact these signatures remain in spectra taken after the I_2 and O_3 flows into the flow tube were shut off.

The I_2 concentration is high when $[O_3]$ is not at its maximum; this generally causes signal saturation in ion counting mode (gap in the data around m/z 254 in Fig. 2a). When such saturation is severe, no useful data can be gathered (the analogue mode can be used instead, see below). However, the atomic iodine signal (Fig. 3b) is generally representative of the I_2 signal due to I_2 fragmentation. This iodine signal (m/z 143) also shows signs of counting saturation due to the large amounts of I_2 in the system at low O_3. Note that atomic iodine generated in the flow tube is quickly scavenged by the large amounts of O_3 present, so its concentration is low. The centre of the IO peak (m/z 143) appeared to be distorted in some experiments; in these cases the peak was fitted with a Gaussian function in order to obtain the integrated area under the peak and preserve the relative scaling with the rest of the I_xO_y integrated peak signals. The maximum IO concentrations in the flow tube are of the order of 10^{12} - 10^{13} molecule cm^{-3}, which should not cause counting saturation. In the analysis (see below) the large IO^+ signal is interpreted as a result of fragmentation of larger molecules. The IO data in Fig. 3 and Fig. 4 are corrected for overload effects and shown at the same relative

View Article Online
DOI: 10.1039/C3CP51217G

scaling observed in the original spectra. The OIO peak (m/z 159) and the other smaller peaks are not distorted and no correction was needed.

The observed decay of the I_2 signal recorded in analogue mode (m/z 254 or m/z 127 for the I^+ fragment) in the presence of different concentrations of O_3 (Fig. 5) yields a rate coefficient $k(298\ \mathrm{K}) = (3.2 \pm 0.5) \times 10^{-18}$ molecule^{-1} cm^3 s^{-1}, in reasonable agreement with the only previous determination $k(298\ \mathrm{K}) = (4.0 \pm 2.0) \times 10^{-18}$ molecule^{-1} cm^3 s^{-1} of the rate coefficient of the slow, spin forbidden gas phase reaction between I_2 and O_3:[26]

$I_2 + O_3 \rightarrow IO + I + O_2$ $(\Delta_r H^0_{298K} = 25\ \mathrm{kJ\ mol^{-1}})$ (R12a)

$I_2 + O_3 \rightarrow IO + OIO$ $(\Delta_r H^0_{298K} = 36\ \mathrm{kJ\ mol^{-1}})$ (R12b)

$I_2 + O_3 \rightarrow IIO + O_2$ $(\Delta_r H^0_{298K} = -68\ \mathrm{kJ\ mol^{-1}})$ (R12c)

$I_2 + O_3 \rightarrow IOI + O_2$ $(\Delta_r H^0_{298K} = -122\ \mathrm{kJ\ mol^{-1}})$ (R12d)

where the enthalpies of reaction have been calculated using experimental values of the enthalpies of formation of $I(^2P_{3/2})$, $I_2(^1\Sigma_g^+)$ and $O_3\ (^1A_1)$ [38], IO $(^2\Pi_{3/2})$ [39] and $OIO(^2B_1)$,[16] and the present calculations at the CCSD(T)//MP2 level of theory for the stable molecules IIO $(^1A')$ and IOI $(^1A_1)$.[31]

Potential products of R12 in the mass spectra include IO (m/z 143), IO_2 (m/z 159) and I_2O (m/z 270) (Fig. 2). The IO dimer, I_2O_2 (IOIO) m/z 286 is generated by R3b with a ~0.3 branching ratio in 100 Torr of N_2,[15] and it is relatively stable at this pressure according to calculations reported in the literature (lifetime >3 seconds).[16] Collisions with He are less effective in stabilising molecular aggregates than with N_2, which reduces the amount of I_2O_2 formation by about a factor of 2, but does not explain why the I_2O_2 peak is minor compared to that of OIO. I_2O_3 (m/z 302) and I_2O_4 (m/z 318) are likely to be formed by R4 and R5 respectively. Reactions R3-R5 are relatively fast at 298 K and 100 Torr ($k > 1 \times 10^{-11}$

View Article Online
DOI: 10.1039/C3CP51217G

molecule^{-1} cm^{3} s^{-1}).[15] However, all the key species have a very similar dependence on [O_3] with effective growth rate constants of the order of ~5 × 10^{-18} molecule^{-1} cm^{3} s^{-1}, as a result of IO, precursor to all of them, being formed in the rate limiting reaction R12.

Very little I_2O_5 (m/z 334) is seen compared to I_2O_4, which seems to indicate that the oxidation path (R9) is minor. However, this observation must be treated with caution, since the calculated ionisation potential of I_2O_5 (Table 1) is above the photon energy of the 118 nm laser radiation, which could imply that the photo-ionisation cross section of I_2O_5 is significantly smaller than that of I_2O_4 at this wavelength. The fact that I_2O_5 still ionises to some extent at this wavelength could be due to the internal energy of the molecule.

The I_3O_y mass peaks ($y \leq 7$) are minor as shown in Fig. 2. Among these, I_3O_6 (m/z 477) and I_3O_7 (m/z 493) are the highest mass signals observed and the most prominent, but while the former does not change with O_3, the latter does in a similar manner to the IO_y and I_2O_y mass signals (Fig 2c). Also the very weak mass I_3O_5 changes in a similar manner to the I_3O_7 species. No mass signals larger than I_3O_7 are observed.

Other mass signals appearing in the mass spectrum in Fig. 1 between m/z 28 and m/z 58 are related to acetone and its fragments. Acetone was used prior to experiments to clean the system and for signal optimisation purposes (it has a large photo-ionisation cross section). A persistent peak appears at m/z 204. This mass does not fit to the I_xO_y pattern and does not have a systematic dependence on [O_3]. It is possibly related to the halocarbon wax coating the flow tube, employed to reduce wall losses.

4. *Ab initio* and rate theory calculations

DOI: 10.1039/C3CP51217G

In order to estimate aggregation rate coefficients between iodine oxides (Table 2), we have first explored potentially stable iodine oxide aggregates by calculating bond energies at the CCSD(T)//MP2 level of theory. The general weakness of the I_3O_y peaks in the mass spectra indicates that IO and OIO do not attach very efficiently to I_2O_y, and suggests that OIO is not the nucleating monomer as proposed in R6. We have performed quantum chemical calculations on a number of I_3O_y conformers with y = 4,...,7, and have found that most of these species are very weakly bound (Table 2 shows bond dissociation energies of the most stable I_3O_y, y = 4,...,7 conformers). In particular, the I_3O_7 species investigated are bound by only ~50 kJ mol^{-1}, which suggest that this mass, clearly varying with $[O_3]$, is most likely a fragment of a larger aggregate. Also, it must be noted that the I_3O_y species have an unpaired electron and are expected to be very reactive. An extensive study has been carried out on aggregates containing 4 iodine atoms, which is detailed in the accompanying paper.[31]

Rate coefficients for the association and dissociation reactions of various I_xO_y species (Table 2) have been calculated using the Master Equation Solver for Multi-Energy well Reactions (MESMER),[40, 41] taking MP2/ECP/aVZT rotational constants and vibrational frequencies, and the CCSD(T)//MP2/ECP/aVZT zero point corrected energies (B3LYP was used instead of MP2 for some calculations involving 4 iodine atoms, due to computational costs).[31] The ro-vibrational energy levels in the *ab initio* potential energy surface are grouped into energy grains, and the population in each grain is described by a set of coupled differential equations that account for collisional energy transfer within each grain as well as dissociation. Microcanonical rate coefficients for the unimolecular reactions that occur in each energy grain are calculated from the *ab initio* data. For barrierless association reactions such as the recombination of iodine oxides, the Inverse Laplace Transform method[42, 43] can be applied to calculate the microcanonical association rates from an estimate of the high pressure limiting rate coefficient for association, assumed to be equal to the collision number and temperature

View Article Online
DOI: 10.1039/C3CP51217G

independent. The microcanonical dissociation rate coefficients are then determined by detailed balance. The exponential down model is used for describing collisional energy transfer probabilities ($\Delta E_{\mathrm{down}} = 250$ cm^{-1}). Lennard-Jones parameters for the interaction of the aggregates with the bath gas (He) are estimated following the procedure recommended by Gilbert and Smith[44] (σ ranging from 5 to 7 Å, ε = 300 K). Parameter selection is guided by a fit to the available experimental data for the IO self-reaction rate coefficient and branching ratios.

5. Discussion

R12 is the initial precursor to the iodine oxides observed in this study. R12a could proceed via formation of a very short lived IOO(^{2}A″) intermediate,[45, 46] and its endothermicity is consistent with the activation energy of 25.0 ± 1.2 kJ mol^{-1} observed for R12.[26] R12b and R12d require insertion of an oxygen atom and therefore are expected to present barriers. Chanel R12c should in principle be the dominant exit channel in view of its exothermicity, but the weakness of the m/z 270 peak (I_2O) and the dominance of the m/z 143 peak (IO) in our spectra (Fig. 3) suggests that there is also a barrier in this channel. In fact, it is likely that the m/z 270 signal results at least in part from photo-fragmentation of I_2O_y. Given the instability of IOO (bond energy 10-20 kJ mol^{-1})[45, 46] and the endothermicity of R12b, the peak at m/z 159 is most likely due to the stable IO_2 isomer, OIO. OIO is generated from the IO self reaction (R3),[15] and could also be produced by the slow reaction ($k \leq 5.0 \times 10^{-16}$ molecule^{-1} cm^3 s^{-1}):[47]

$$IO + O_3 \rightarrow OIO + O_2 \qquad (\Delta_r H^0_{298K} = -145.6 \text{ kJ mol}^{-1}) \qquad \text{(R13)}$$

View Article Online
DOI: 10.1039/C3CP51217G

Note however that for the estimated IO peak concentration of ~10^{13} molecule cm^{-3}, the first-order rate of IO removal (to form OIO) by R3 is ~800 s^{-1}, while IO removal (to form OIO) via R13 with $[O_3]$ ~ 10^{16} molecule cm^{-3} would only proceed at ~ 5 s^{-1}.

Kinetic Modelling

Based on the observations above, kinetic modelling of the chemistry initiated by R12 has been carried out in order to achieve a coherent picture of the mass spectra. Since simple kinetic modelling shows that the dependence on O_3 of all species is to a large extent determined by R12, the objective of this modelling is explaining the relative intensities of the different peaks. Using experimental and calculated rate coefficients with He as the bath gas (Table 2) and the initial concentrations of I_2 and O_3, the model is integrated using a solver of stiff differential equations.[48] The simulated data is globally fitted to the key species observed (IO, OIO, I_2O_2, I_2O_3, I_2O_4 and I_2O_5) using a non-linear least squares algorithm, by floating selected concentration scaling factors and/or rate coefficients, as well as a first order loss rate to account for wall losses and aerosol uptake of all these species. No explicit weighting is applied to the data, although in such a global fit the original relative scaling of the different observed signals ($S_{IO} > S_{OIO} > S_{I2O4} > S_{I2O2} \approx S_{I2O3}$) implies that the most prominent peaks carry more weight in the fit.

In the simplest modelling case (Fig. 4a-4f), the following assumptions are made:

1) The photo-ionisation cross sections at 118 nm of the observed I_xO_y species are the same and no fragmentation takes place. This implies that the relative signals are assumed to be representative of the relative concentrations.
2) The chemical mechanism is well defined (bold case reactions in Table 2)
3) All I_xO_y are lost to the walls (or aerosols) with the same efficiency.

Thus, a common concentration scaling factor to convert signal into concentration is fitted alongside the wall loss rate, and all the literature and calculated rate constants are fixed. This exploratory modelling exercise allows us to assess which processes are defined and which assumptions in the model may be deficient. The I_2O_2 and I_2O_3 signals are an order of magnitude too small compared with the simulated concentrations (Fig. 4c and 4d). Another important observation is that the model does not produce enough OIO and I_2O_4 to match the observed signal (Fig. 4b and 4e). This could result from an insufficient mechanistic description in the model (i.e. reactions missing in Table 2) and/or poor estimates of the kinetic parameters for R3-R5 and R7-R9. However, this situation could be also resolved if assumption 1 is removed, i.e. if photo-ionization cross-sections are larger for OIO and I_2O_4 compared to I_2O_2 and I_2O_3. It is also likely that fragmentation of I_2O_2 and I_2O_3 contributes to enhance the IO and OIO signals.

Effect of photo-ionisation and photo-fragmentation

In general, for any observed peak at m/z i (note we consider here only singly ionised species and 1 photon processes) the TOF integrated peak signal S_i can be expressed as the sum of contributions from the photo-ionisation of the neutral parent mass associated to i ($j=i$) and all other ($j > i$) neutral species fragmenting to i:

$$S_i = K \times E \times \sum_j \sigma_j(\lambda) \times \phi_{ij}(\lambda) \times [j] \qquad \text{(E1)}$$

where K is a constant characteristic of the instrument, E is the laser pulse energy, $\sigma_j(\lambda)$ is the total photo-ionisation cross section of species j at the laser wavelength λ, $\phi_{ij}(\lambda)$ is the ionic photo-fragmentation branching ratio for production of m/z i from neutral j (including $j = i$) and $[j]$ is the concentration of the neutral species with mass j.[49] When the concentration time-

View Article Online
DOI: 10.1039/C3CP51217G

profiles are very similar as in the present case (R12 rate limiting) then we have $[i] \propto [j]$ for all ozone concentrations, and (E1) reduces to:

$$S_i \approx K \times E \times [i] \times \sum_j \sigma_j(\lambda) \times \phi_{ij}(\lambda) \times R_{ij} = C_i \times [i] \qquad \text{(E2)}$$

where $R_{ij} = [j] / [i]$. In summary, a PI-TOF-MS signal at m/z i can appear to be larger than others not only due to a larger $[i]$, but also as a result of a larger photo-ionisation cross section and/or branching ratio of the parent mass ($j = i$), or to the addition of further contributions from fragmentation of neutral species with larger m/z ($j > i$), resulting in an enhanced C_i. It must be remembered that in general the approximation made in E2 is not applicable in all cases: when the different signals present different kinetic behaviour, the overlap of parent and fragment signal causes C_i being dependent on reaction contact time or reactant concentration (O_3 in our case). In that case, a $C_i(t, [O_3])$ needs to be fitted for every time or concentration, or alternatively the effective cross sections $\sigma_j \times \phi_{ij}$ in E1 would need to be independently fitted. This problem resembles the overlap of optical absorption signals, and has been addressed in previous studies by using a tuneable photo-ionisation source.[50]

Panels (g)-(l) in Fig. 4 show the results of a second modelling case where, following E2, the scaling factors for IO, OIO, I_2O_2, I_2O_3 and I_2O_4 are allowed to float independently in order to fit the observations (i.e. assumption 1 is removed). C_{I2O5} is initially fixed to be equal to C_{IO} due to the low weight of S_{I2O5} in the fit. The fitted concentration scaling factors are shown in the lower right corner of each panel of Fig. 4. In principle, it would be possible to feed back the C_i obtained from the fit into E2, to derive cross sections σ_j and branching ratios ϕ_{ij} from a system of equations. This requires however a calibration of the instrumental factor to determine K and E and, in addition, a number of assumptions would need to be made in order to reduce the number of unknowns to the number of equations. The first fragmentation ion is usually coming from dissociation of the weakest bond in the parent molecule, where the ion signal is from the most ionisable dissociation fragment. Therefore it is reasonable to expect the following fragmentation:

$I_2O_2 + h\nu \rightarrow [I_2O_2^+]^* + e^-$; $[I_2O_2^+]^* \rightarrow IO^+ + IO$

$I_2O_3 + h\nu \rightarrow [I_2O_3^+]^* + e^-$; $[I_2O_3^+]^* \rightarrow IO^+ + OIO$

$I_2O_4 + h\nu \rightarrow [I_2O_4^+]^* + e^-$; $[I_2O_4^+]^* \rightarrow OIO^+ + OIO$

where $[I_2O_y^+]^*$ (y = 2-4) are molecular ions in an electronic excited state.[49] But the extent of fragmentation is difficult to theoretically predict. Even though this could not be accomplished in the present study, the ratios between the C_i values provide some information about photo-ionisation. The particular exercise in Fig. 4 yields $C_{I2O2} \sim C_{IO}/18$ and $C_{I2O3} \sim C_{IO}/61$, which suggests that the parent molecules I_2O_2 and I_2O_3 are fragmenting extensively rather than due to small total ionization cross-sections, i.e. ϕ_{ii} (branching ratios for the parent neutral species) are small compared with ϕ_{ij} (photo-fragmentation branching ratios). The ratio $C_{I2O4} \sim C_{OIO}/1.6$ is much smaller than the above ratios and therefore suggests that I_2O_4 ionizes with much less fragmentation compared to I_2O_2 and I_2O_3. If the above fragmentation schemes are operating, i.e. fragmentation via the weakest bond, then the suggestion that I_2O_2 and I_2O_3 are fragmenting to a greater extent than I_2O_4 is borne out by the fact that the scaling factor for IO is 1.4 times larger than for OIO. It is possible as well that the I_2O signal (m/z 270) corresponds to photo-fragmentation of I_2O_y rather than originating from R12c. Although I_2O has not been included in the model, this signal could be also accounted for including a small branching (~2%) for channel R12c and assuming $C_{I2O} \approx C_{IO}$, without affecting significantly the results for the major species. Fragmentation of higher oxides could also contribute to enhance S_{I2O4} relative to S_{I2O2} and S_{I2O3}.

View Article Online
DOI: 10.1039/C3CP51217G

Sensitivity to kinetic parameters

An explanation for the small I_2O_y signals alternative to photo-fragmentation could be chemical or aggregation reactions of these species (i.e. keep assumption 1 and remove assumption 2). Our quantum calculations and previous theoretical studies[16, 51] show that the thermal decomposition of I_2O_2, I_2O_3 and I_2O_4 is too slow to cause significant loss on the time scale of tens of seconds. The absence of large, ozone-dependent I_3O_y (y = 3,...,5) signals suggest that aggregation of I_2O_2 and I_2O_3 with IO and OIO is not favoured, and in fact our calculations indicate that the I_3O_y aggregates are not strongly bound (see bond dissociation energies in Table 2) . Slow rate coefficients for R7-R9 have been considered so far (assumed to be the same as for R13) (Table 2). Our modelling shows that R7 would need to be as fast as 1×10^{-13} $\text{molecule}^{-1}\ \text{cm}^3\ \text{s}^{-1}$ to at least match the order of magnitude of the observed I_2O_2 signal when assumption 1 is considered, and in addition the O_3 dependence would go in the wrong direction (Fig. 4d shows an I_2O_2 simulated trace for this fast oxidation case). Moreover, it is not possible to fit successfully the data considering the same rate constant for R7-R9, and therefore we infer that these reactions are not responsible for the relative signals observed. Finally, a modelling case where the rate coefficients of R4 and R5 and the branching ratios of R3 are floated along with a single common scaling factor produces a satisfactory fit. However, the optimal values of k_{3b}/k_3 and k_4 resulting from this exercise are one order of magnitude lower than our estimated values included in Table 2, which are based on a combination of experiments in N_2[15] and rate theory calculations (see below). It can be concluded that, although there is some degree of uncertainty in the kinetic parameters of this fairly simple chemical system (factor of 2, based on the variation of different parameters in the rate theory calculations with MESMER), the observed PI-TOF-MS signals are to a large extent determined by photo-ionisation and photo-fragmentation.

View Article Online
DOI: 10.1039/C3CP51217G

The sensitivity to the variation of key kinetic parameters within the range of estimated uncertainty is summarised in Table 3, where the effect on the fitted photo-ionisation scaling factors, the loss rate and goodness-of-fit parameter χ^2 are shown ($\chi^2 = 4.5$ for the base case in Table 2 and Fig. 4g-4l). The model is run using always the same chemical scheme shown in Table 2, but for different values of the kinetic parameters relevant to the I_2O_y species spanning their range of estimated uncertainty, and the percentage of variation of each C_i with respect to the base case run is calculated. For reactions R7-9 a common rate coefficient is assumed and varied over 2 orders of magnitude with the objective of obtaining an upper limit of this parameter. Doubling (runs 1, 3 and 5) or halving (runs 2, 4 and 6) the values of k_{3b}/k_3, k_4 and k_5 does not have a big impact in the quality of the fit. The C_i coefficients change to accommodate such variations, and in most cases these variations overlap with the parameter error estimates of the base case fit, which highlights the need of different kinetic traces to obtain more information from this kind of system (i.e. find a source reaction which is not rate limiting).

Including R7-9 in the model (model runs 7, 10 and 13) notably changes the quality and also leads to an over-parameterised fit, as revealed by large errors of the fitted parameters. It can be seen that $k_{7\text{-}9} = 1 \times 10^{-13}$ molecule^{-1}cm^{3}s^{-1} increases significantly the value of χ^2. The fit quality is also poorer even with $k_{7\text{-}9} = 5 \times 10^{-15}$ molecule^{-1}cm^{3}s^{-1}, only a factor of 10 higher than the value assumed in Table 2. Such increases in χ^2 result from a poorer fitting of the I_2O_y species, and also partially from the larger amounts of I_2O_5 generated in the model, which are not consistent with I_2O_5 having the same C_i as IO. The loss rate increases as well to compensate for the fast growth of I_2O_5. This poorer fitting reflects the fact that at some point reactions R7-9 start having an influence on the dependence of I_2O_y on ozone. If the scaling factor C_{I2O5} is allowed to vary (runs 8, 11 and 14), χ^2 comes reasonably close to the base case value (5.08) when $k_{7\text{-}9} = 5 \times 10^{-15}$ molecule^{-1}cm^{3}s^{-1}. In a separate set of runs (9, 12 and 15)

View Article Online
DOI: 10.1039/C3CP51217G

S_{I2O5} is excluded from the observational vector. Although the χ^2 values of these three runs are not comparable to the rest, the trend of decreasing χ^2 with decreasing $k_{7\text{-}9}$ is clear. From this sensitivity analysis a conservative upper limit of $k_{7\text{-}9} < 1 \times 10^{-14}$ molecule^{-1}cm^{3}s^{-1} can be deduced based on the marginal difference in quality between runs 11 and 14.

Link to IOP formation

We have used the model run 11 (Table 3) ($k_{7\text{-}9} = 1 \times 10^{-14}$ molecule^{-1} cm^3 s^{-1}) to make an assessment of what is the most likely step after formation of the I_2O_y molecules. Fig. 6 shows the time dependence of the major species generated by the chemical mechanism for a model run with [O_3] ~ 2×10^{16} molecule cm^{-3}. The dashed lines indicate the contact time corresponding to the spectra in Fig. 2b and 2d and show how the relative signals would change significantly in time. In particular, this implies distortion of the IO parent mass signal at shorter contact times by fragmentation of I_2O_2 and I_2O_3. These two oxides are formed at high concentrations, but according to our quantum calculations, they do not form any stable aggregate, and therefore they will be simply lost to walls or taken up by aerosol. By contrast, I_2O_4 forms a stable aggregate, I_4O_8. The insert panel in Fig. 6 shows that when the C_{I2O4} scaling factor is applied to the I_3O_7 signal observed, the agreement between scaled signal and modelled concentration is remarkably good. Although this is far from an unambiguous assignment, it suggests that the I_3O_7 signal is likely to result from I_4O_8 fragmentation, also considering that there are no other I_xO_y species at a sufficiently high concentration to generate such fragment. Alternatively, I_3O_7 could result from fragmentation of IOPs formed by the attachment of any other I_xO_y to I_4O_8.

Finally, it is worth paying some attention to the fate of I_2O_5. When the upper limit for $k_{7\text{-}9}$ is considered, significant concentrations of I_2O_5 are generated by the model (~ 1×10^{10} molecule cm^{-3}), which may appear in the experiments as a small S_{I2O5}, possibly as a result of a below-threshold photo-ionisation cross section. Species with high enough concentration to be potentially important sinks for I_2O_5 are IO, OIO and I_2O_3. However, our calculations indicate that they do not form stable bonds with I_2O_5. In particular, the different conformers of the $I_2O_5\cdots OIO$ adduct are too weakly bound, so this has to be discounted as a potential sink (as well as an explanation of the I_3O_7 signal). Thus, I_2O_5 is a minor species compared to I_2O_2 and I_2O_3, with a similar inability to form stable homo- or heterodimers, apart from I_4O_9. Its main fate could be hypothesised as well as wall loss and uptake by the growing IOP population descending from I_4O_8. It is difficult to envisage a path from gas phase I_2O_5 to the solid particles of this composition reported in the literature.[21, 23] This would necessarily involve a preferential uptake of I_2O_5 by I_4O_8, I_4O_9 and by the aggregates subsequently formed in order to gradually increase the O:I stochiometric ratio of the IOPs to values closer to 2.5. However, the fact that particles form in the absence of ozone[23] suggest that gas phase I_2O_5 does not play any special role.

6. Conclusions

The products of the slow $I_2 + O_3$ reaction in the dark have been found to be mainly I and IO, generated by a slightly endothermic channel. The use of this reaction as precursor of iodine oxides in a high pressure-slow flow tube equipped with PI-TOF-MS has been shown to be a promising approach for studying the first steps of iodine oxides nucleation and their photochemistry. For the first time direct observation of key gas-phase I_xO_y species with $x \geq 2$ has been reported. Ozone is unlikely to make a major contribution to the formation of I_2O_y, since the dependence on O_3 of the I_2O_y species is inconsistent with fast oxidation reactions. A conservative upper limit to the rate constant of ozone oxidation steps has been derived ($k_{7\text{-}9} < 1 \times 10^{-14}$ molecule^{-1}cm^{3}s^{-1}), which rules out the evolution of I_2O_5 stoichiometry IOPs directly from I_2O_5 gas phase nucleation.[21, 23] The relative intensity of the PI-TOF-MS signals

View Article Online
DOI: 10.1039/C3CP51217G

observed has been mainly attributed to photo-fragmentation, which is severe in the case of I_2O_2 and I_2O_3 at 118 nm.

I_3O_y (y < 6) species do not form in significant amounts in the gas phase. In view of the instability of aggregates involving I_2O_2 and I_2O_3 indicated by our quantum calculations, the dimerisation of I_2O_4 is likely to be the key reaction at this stage, considering the unusual stability of the I_4O_8 aggregate. I_4O_8 should probably be regarded as the smallest IOP. I_2O_2 and I_2O_3 are dead ends in the nucleation mechanism, but they possibly attach to I_4O_8. A fragment with I_3O_7 stoichiometry is observed, which can be related either to I_4O_8 or to clusters formed by the aggregation of I_4O_8 and any other I_xO_y. Even though I_2O_5 has an IP above the photo-ionisation energy employed in this study according to our quantum calculations, it seems to play a marginal role in view of the slow ozone oxidation rate coefficients. The I_2O_5 composition of particles previously reported is therefore likely a result from I_2 liberation in the solid-phase.

Further work is needed to improve the sensitivity and reproducibility in the experimental system – especially regarding blocking of the pinhole and reduction of wall losses, in order allow a wider range of concentrations, pressures and contact times. Also, tuneable ionisation radiation could be used to avoid fragmentation of I_2O_2 and I_2O_3. Future studies using the I_2 + O_3 synthesis method should focus on the determination of the photochemical properties of I_xO_y, which is one of the largest uncertainties in atmospheric iodine models.[6]

Acknowledgements

This work was supported by the Natural Environment Research Council (grant NE/E005659/1). O. G. acknowledges financial support from Ministerio de Ciencia e Innovación, "Ramón y Cajal" program, and Project FIS2010-16455

Tables

View Article Online
DOI: 10.1039/C3CP51217G

Table 1. Ionization potentials of atomic and molecular iodine and of iodine oxides

Ion	**m/z**	**Ionization energy (eV) / Wavelength (nm)**		
		Literature (Experimental)	**Literature (Theoretical)**	**This work (Theoretical [d])**
$I^+(^3P)$	127	10.451 [a] / 118.7		10.35 / 119.9
$HI^+(^2\Sigma)$	128	10.381 [a] / 119.5		10.50 / 118.2
$I_2^+(^2\Sigma)$	254	9.3995 [a] / 132.0		9.47 / 131.0
$IO^+(^3\Sigma)$	143	9.745±0.017 [b] / 127.3		9.56 / 129.8
$OIO^+(^1B)$	159		9.793 [c] / 126.7	9.72 / 127.6
$IIO^+(^2A)$	270			9.02 / 137.5
$IOIO^+(^2A)$	286			9.13 / 135.9
$OI(I)O^+(^2A)$	286			10.38 / 119.5
$I_2O_3^+ (^2A)$	302			9.97 / 124.4
$I_2O_4^+ (^2A)$	318			9.26 / 134.0
$I_2O_5^+(^2A)$	334			11.38 / 108.9
$I_3O_5^+(^1A)$	461			9.46 / 131.1
$I_3O_6^+(^1A)$	477			9.06 / 136.9
$I_3O_7^+(^1A)$	493			8.69 / 142.8

[a] JANAF tables [52]. [b] Reference [53]. Given as adiabatic [c] Reference [54]. Given as adiabatic. Estimation based in the performance of different levels of theory on the reproduction of the experimental ionization potentials of OClO and OBrO [d] CCSD(T)//MP2/AREP/aVTZ. Given as vertical.

View Article Online
DOI: 10.1039/C3CP51217G

Table 2. Chemical Mechanism (T = 298 K, P = 100 Torr)

R#	Reaction [a]	k / molecule^{-1}cm^{3}s^{-1}		Reference/Notes
2	**$I + O_3 \rightarrow IO + O_2$**	1.3×10^{-12}		[55]
3a	**$IO + IO \rightarrow I + OIO$**	7.0×10^{-11}		[15 c]
3b	**$IO + IO \rightarrow I_2O_2$**	1.0×10^{-11}		[15 c]
4	**$IO + OIO \rightarrow I_2O_3$**	4.2×10^{-11}		Calculated [d,e]
5	**$OIO + OIO \rightarrow I_2O_4$**	1.7×10^{-11}		Calculated [e]
7	$I_2O_2 + O_3 \rightarrow I_2O_3 + O_2$	5.0×10^{-16}		Assumed (R13)
8	$I_2O_3 + O_3 \rightarrow I_2O_4 + O_2$	5.0×10^{-16}		Assumed (R13)
9	$I_2O_4 + O_3 \rightarrow I_2O_5 + O_2$	5.0×10^{-16}		Assumed (R13)
12a	**$I_2 + O_3 \rightarrow I + IO + O_2$**	3.2×10^{-18}		Exp. decay, this work
13	$IO + O_3 \rightarrow OIO + O_2$	5.0×10^{-16}		[47]
15	$I_2O_4 + IO \rightarrow I_3O_5$	1.5×10^{-11}		Calculated
16	$I_2O_4 + OIO \rightarrow I_3O_6$	2.8×10^{-12}		Calculated
17	$I_2O_5 + OIO \rightarrow I_3O_7$	1.0×10^{-13}		Calculated
18	$I_2O_3 + I_2O_3 \rightarrow I_4O_6$	1.4×10^{-12}		Calculated
19	$I_2O_3 + I_2O_4 \rightarrow I_4O_7$	2.7×10^{-11}		Calculated
20	$I_2O_3 + I_2O_5 \rightarrow I_4O_8$ (C1)	1.9×10^{-11}		Calculated
21	$I_2O_4 + I_2O_4 \rightarrow I_4O_8$ (C2)	2.7×10^{-10}		Calculated
22	$I_2O_4 + I_2O_5 \rightarrow I_4O_9$	1.2×10^{-11}		Calculated
23	$I_2O_5 + I_2O_5 \rightarrow I_4O_{10}$	7.0×10^{-11}		Calculated
R#	**Reaction**	**D_0 / kJ mol^{-1} [b]**	**k' / s^{-1}**	
24	$I_2O_2 \rightarrow I + OIO$	84	1.2×10^{-3}	Calculated
25	$I_2O_3 \rightarrow IO + OIO$	161	Stable	Calculated
26	$I_2O_4 \rightarrow OIO + OIO$	98	1.1×10^{-2}	Calculated
27	$I_3O_5 \rightarrow I_2O_4 + IO$	62	6.2×10^{4}	Calculated
28	$I_3O_6 \rightarrow I_2O_4 + OIO$	74	3.5×10^{4}	Calculated
29	$I_3O_7 \rightarrow I_2O_5 + OIO$	32	3.7×10^{7}	Calculated
30	$I_4O_6 \rightarrow I_2O_3 + I_2O_3$	58	7.5×10^{5}	Calculated
31	$I_4O_7 \rightarrow I_2O_3 + I_2O_4$	79	1.6×10^{4}	Calculated
32	I_4O_8 (C1) $\rightarrow I_2O_3 + I_2O_5$	86	2.8×10^{3}	Calculated
33	I_4O_8 (C2) $\rightarrow I_2O_4 + I_2O_4$	141	Stable	Calculated
34	$I_4O_9 \rightarrow I_2O_4 + I_2O_5$	107	8.7	Calculated
35	$I_4O_{10} \rightarrow I_2O_5 + I_2O_5$	88	1.9×10^{3}	Calculated
36	**$I_xO_y \rightarrow$ loss**	-	32	Fitted

[a] The key reactions for reproducing observed species in the base case run appear in bold case [b] Dissociation energies of the species at the left hand side of the dissociation reaction have been obtained from *ab initio* calculations at CCSD(T)//MP2/AREP/aVTZ. [c] Corrected for He as bath gas. [d] MESMER calculations use the CCSD(T) dissociation energies D_0 included in the table, vibrational frequencies and rotational constants at MP2/AREP/aVTZ level of theory (except I_4O_7, I_4O_9 and I_4O_{10}, for which the B3LYP/AREP/aVTZ level was used)[31]. Lennard-Jones parameters for interaction with He bath gas taken from ref. [44] and $\Delta E_{down} = 250$ cm^{-1} (T-independent). [e] Rate coefficients in N_2 at 150 Torr are ~ 8×10^{-11} molecule^{-1} cm^3 s^{-1} . The calculations are carried out to reproduced this number and then repeated for He as bath gas.[15]

View Article Online
DOI: 10.1039/C3CP51217G

Table 3. Sensitivity of photo-ionisation scaling factors to kinetic parameters

param	**#**	**δ*k***	**Δ*C*/*C*$_{IO}$** [a]	**Δ*C*/*C*$_{OIO}$**	**Δ*C*/*C*$_{I2O2}$**	**Δ*C*/*C*$_{I2O3}$**	**Δ*C*/*C*$_{I2O4}$**	**Δ*C*/*C*$_{I2O5}$**	**Δ*k*'/*k*'$_{loss}$**	**χ^2** [b]
k_{3b}/k_3	1	×2	3	24	-34	42	30	-	19	4.83
	2	÷2	-1	-6	70	-7	*-5* [e]	-	-1	4.52
k_4	3	×2	8	54	41	9	*48*	-	30	4.77
	4	÷2	-6	-27	-26	*7*	-26	-	-20	4.44
k_5	5	×2	-1	13	-1	*12*	*-14*	-	1	4.57
	6	÷2	1	-8	0	-8	*15*	-	-1	4.47
$k_{7\text{-}9}$	7	×200	108	897 [f]	1885	4831	1038	-	574	5.87
	8	×200 [c]	106	897	1868	4814	1036	-61	*565*	5.69
	9	×200 [d]	108	897	1871	4813	1030	-	572	4.11
	10	×20	105	897	1389	4088	1087	-	567	5.56
	11	×20 [c]	6	17	*154*	*168*	*-1*	*-96*	*19*	5.08
	12	×20 [d]	9	32	*188*	*235*	19	-	*46*	3.90
	13	×10	14	59	*184*	*280*	*64*	-	89	5.38
	14	×10 [c]	4	*9*	83	80	-12	*-94*	9	4.81
	15	×10 [d]	5	16	99	106	-2	-	22	3.60

[a] % change of the fitted coefficient relative to the corresponding result of the base case fit using the kinetic parameters in Table 2 (base case fit coefficients given in Fig. 4g-4l). [b] The base case fit chi-square value is $\chi^2 = 4.5$ [c] An scaling factor C_{I2O5} is also allowed to float. Changes are relative to $C_{IO} = C_{I2O5}$ in the base case fit [d] S_{I2O5} excluded from the fit [e] Italics indicate coefficients with estimated errors larger than 30%. [f] Small typescript indicate coefficients with estimated errors larger than 50%

Figure captions

View Article Online
DOI: 10.1039/C3CP51217G

Figure 1. Panel (a): raw signal vs. time of flight (TOF) (note the logarithmic scale). Panel (b): mass to charge calibration linear fit.

Figure 2. TOF spectra after contact times of 10 s (panel (a)) and 25 s (panel (b)), in each case for O_3 concentrations differing by one order of magnitude (red: $[O_3] \sim 1 \times 10^{15}$ molecule cm^{-3}, black $[O_3] \sim 1 \times 10^{16}$ molecule cm^{-3}). The blue spectra were obtained by averaging respectively 13 and 7 spectra taken at the same contact time. Panels (b) and (d) show the spectra resulting from subtracting the red spectra from the black spectra in the upper panels. The high mass window appears multiplied by 20 on the right hand side panels for clarity. The saturated I_2 peak has been removed from panels (a) and (b) for clarity.

Figure 3. Panel (a): evolution of pressure and ozone concentration during a typical experiment sequence. Panel (b): integrated peak signal for the I, IO and OIO peaks for every experiment. The iodine atom signal corresponds to I_2 fragmentation (O_3 scavenges quickly iodine atoms for the system and these are below detection limit). Note that I and IO are anticorrelated. Panel (c): the same for mass signals showing positive and significant correlation with IO and OIO. Panel (d): the same for mass signals showing negative correlation with IO and positive correlation with I, and negative correlation with pressure.

Figure 4. Results of fitting simulated data (lines) using the model in Table 2 to the observed O_3 dependence of integrated peak signals (symbols). Left panel column (a)-(f): simulated concentrations are fitted to observations with all species having the same floating signal scaling factor. Right panel column (g)-(l): best fit and base case run for sensitivity studies, where circles denote species with a common floating signal scaling factor. Species with other symbols have their own floating scaling factor. Note that panels (c), (d), (i) and (j) are in a logarithmic scale to emphasise the failure of the common scaling factor approach due to the

View Article Online
DOI: 10.1039/C3CP51217G

weak I_2O_2 and I_2O_3 signals. The dashed line in panel (d) is a result of a different fit with common scaling factor and including a fast $I_2O_2 + O_3$ reaction (see text for details).

Figure 5. Pseudo first order decay of the I_2 integrated peak signal recorded in analogue mode (parent ion empty squares and I^+ fragment solid squares). The lines represent linear regressions of the logarithm of the signal vs. the product of ozone concentration and contact time.

Figure 6. Simulated curves (log scale) as a function of contact time for the highest O_3 concentration in Fig 4 (2×10^{16} molecule cm^{-3}). The vertical dashed lines indicate the contact times corresponding to the spectra shown in Fig. 3. The insert panel shows the I_2O_4 and I_3O_7 signals scaled with the I_2O_4 scaling coefficient C_{I2O4}, compared to the model output for I_2O_4 and I_4O_8 as a function of $[O_3]$.

Figures

View Article Online
DOI: 10.1039/C3CP51217G

Figure 1

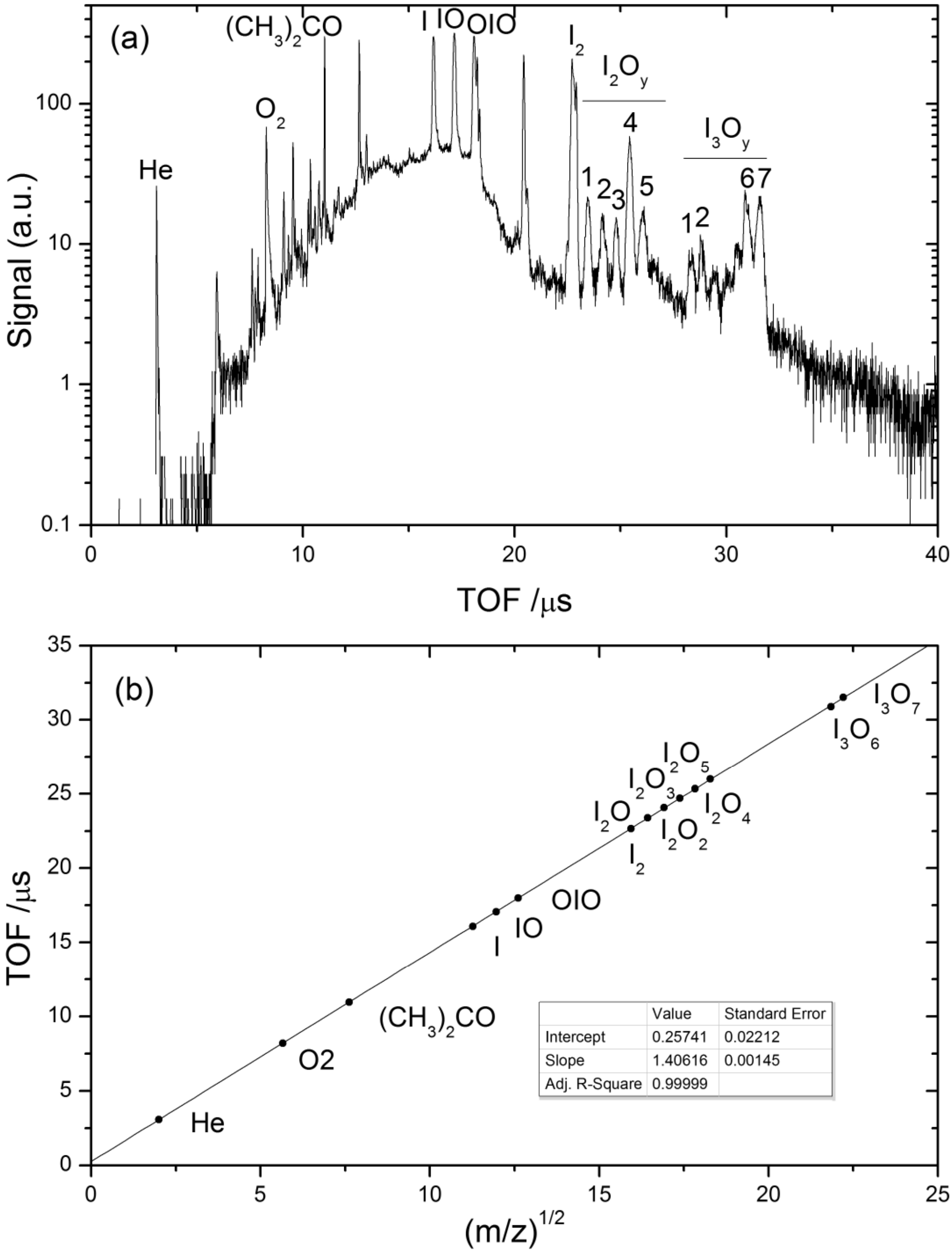

Figure 2

View Article Online
DOI: 10.1039/C3CP51217G

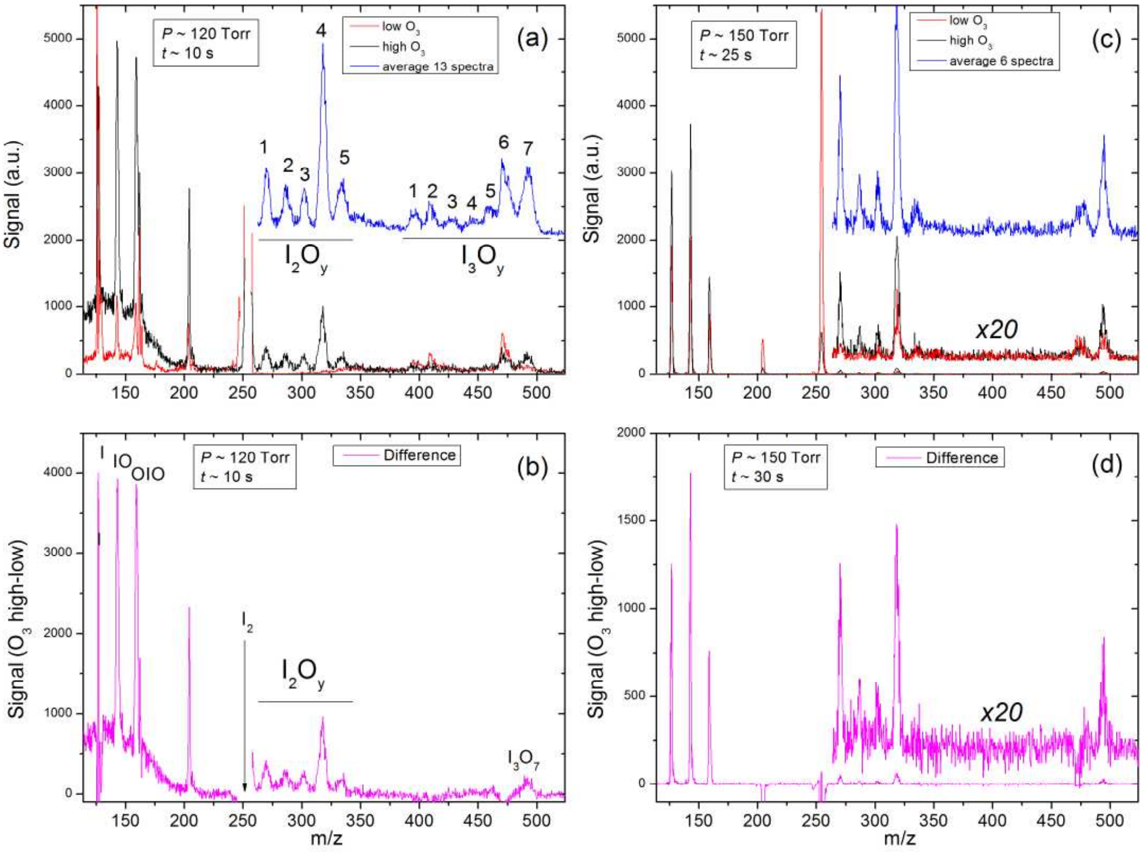

View Article Online
DOI: 10.1039/C3CP51217G

Figure 3

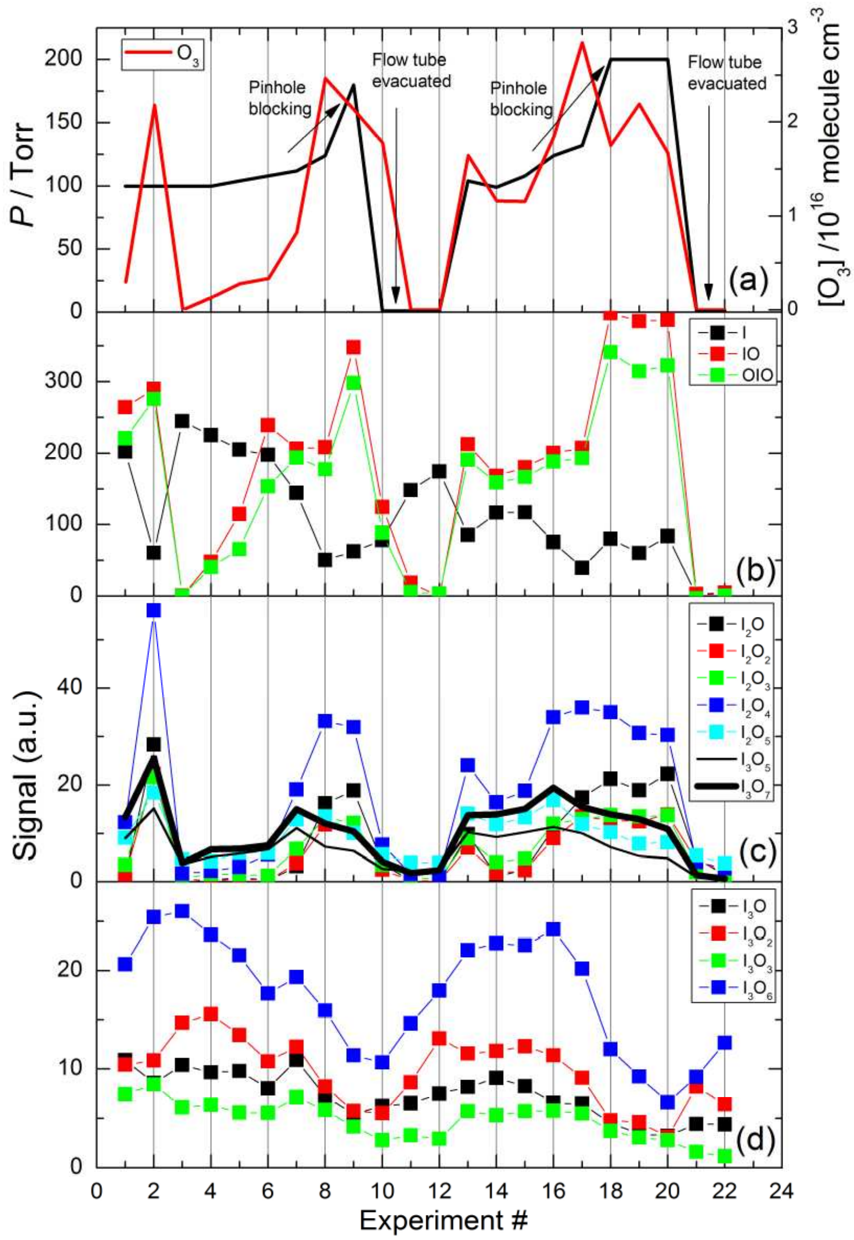

View Article Online
DOI: 10.1039/C3CP51217G

Figure 4

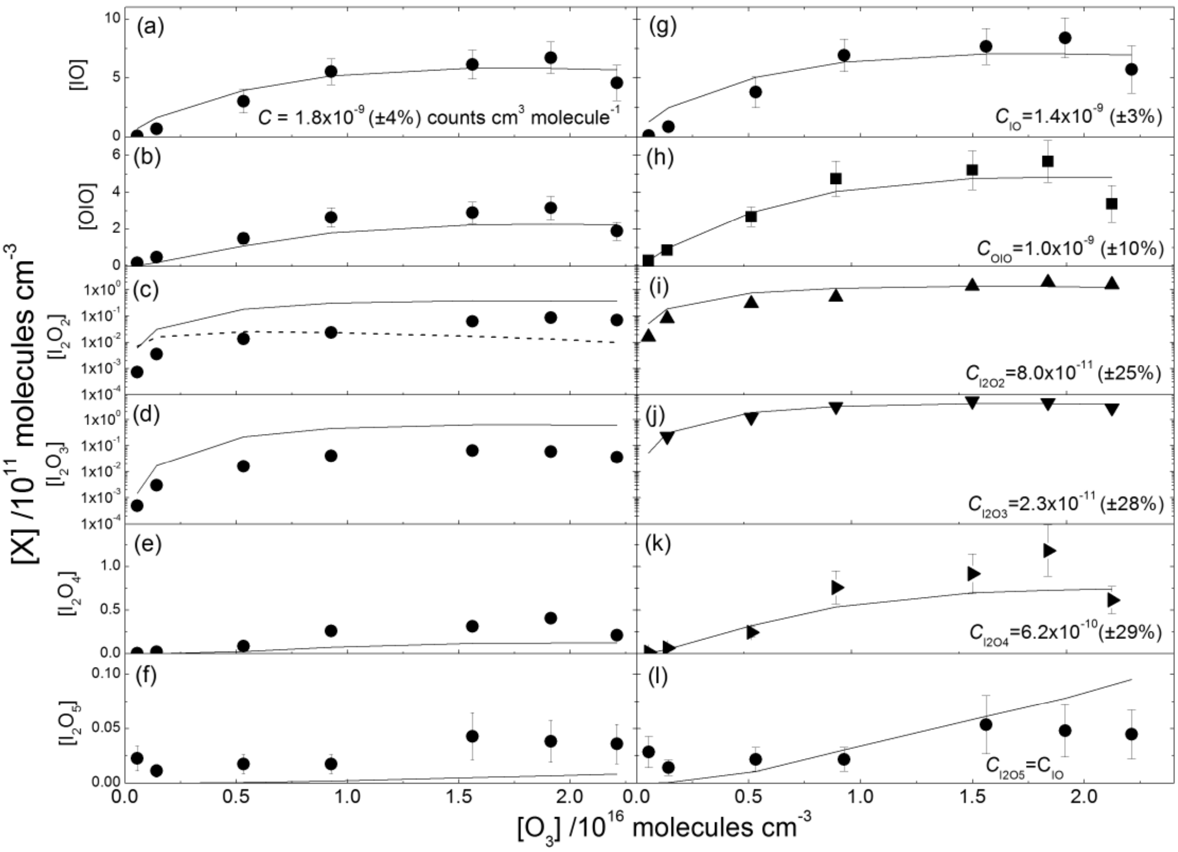

Figure 5

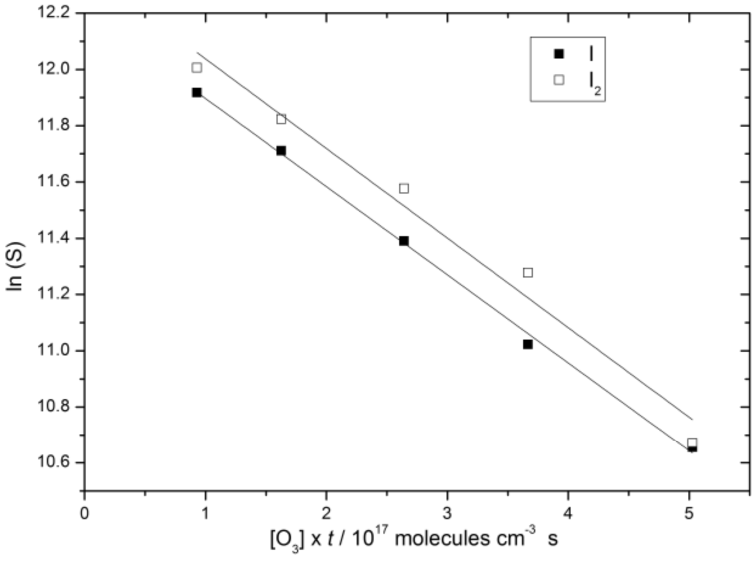

View Article Online
DOI: 10.1039/C3CP51217G

Figure 6

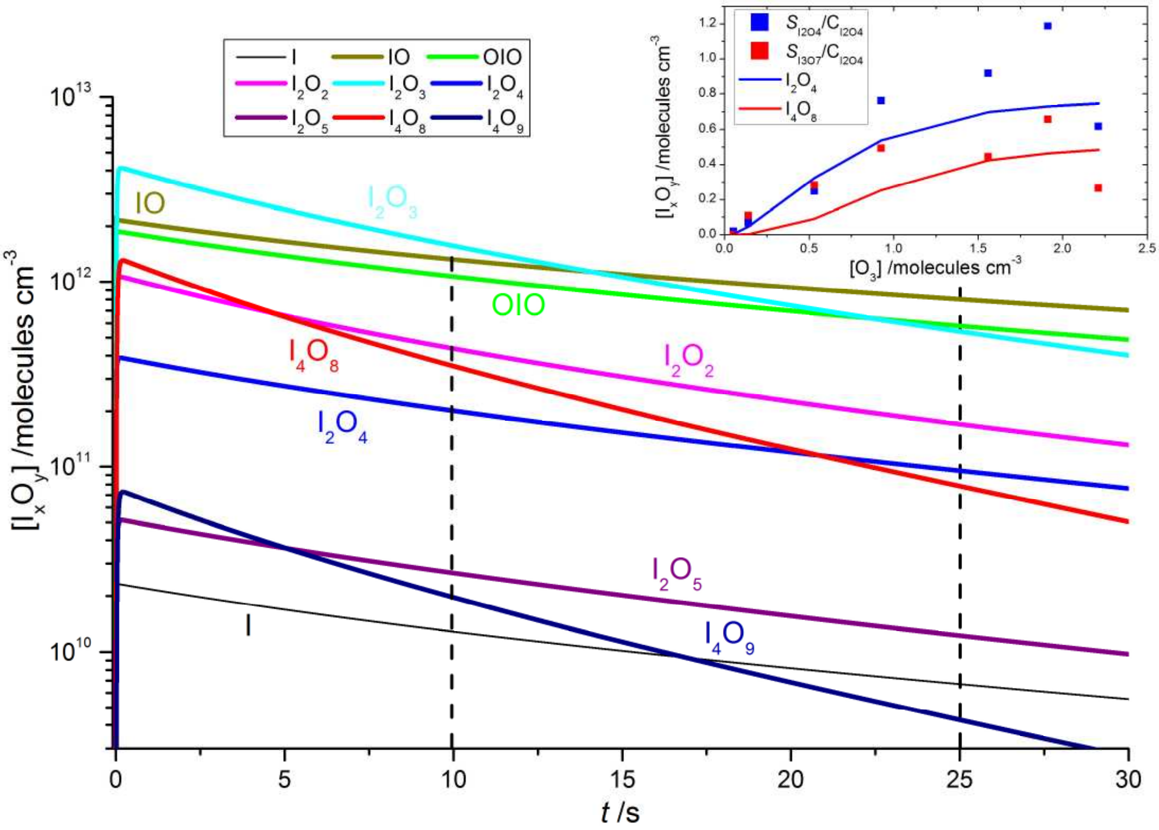

References

View Article Online
DOI: 10.1039/C3CP51217G

1. B. J. Allan, G. McFiggans, J. M. C. Plane and H. Coe, *J. Geophys. Res. [Atmos.]*, 2000, **105**, 14363-14369.
2. A. S. Mahajan, J. C. Gómez Martín, T. D. Hay, S.-J. Royer, S. A. Yvon-Lewis, Y. Liu, L. Hu, C. Prados-Roman, C. Ordóñez, J. M. C. Plane and A. Saiz-Lopez, *Atmos. Chem. Phys.*, 2012, **12**, 11609-11617.
3. K. A. Read, A. S. Mahajan, L. J. Carpenter, M. J. Evans, B. V. E. Faria, D. E. Heard, J. R. Hopkins, J. D. Lee, S. J. Moller, A. C. Lewis, L. Mendes, J. B. McQuaid, H. Oetjen, A. Saiz-Lopez, M. J. Pilling and J. M. C. Plane, *Nature*, 2008, **453**, 1232-1235.
4. A. Saiz-Lopez, A. S. Mahajan, R. A. Salmon, S. J.-B. Bauguitte, A. E. Jones, H. K. Roscoe and J. M. C. Plane, *Science*, 2007, **317**, 348-351.
5. A. Saiz-Lopez and J. M. C. Plane, *Geophys. Res. Lett.*, 2004, **31**, L04112.
6. A. Saiz-Lopez, J. M. C. Plane, A. Baker, L. Carpenter, R. von Glasow, J. C. Gómez Martín, G. McFiggans and R. Saunders, *Chem. Rev.*, 2012, **112**, 1773–1804.
7. R. A. Cox and G. B. Coker, *J. Phys. Chem.*, 1983, **87**, 4478-4484.
8. M. H. Harwood, J. B. Burkholder, M. Hunter, R. W. Fox and A. R. Ravishankara, *J. Phys. Chem. A*, 1997, **101**, 853-863.
9. M. E. Jenkin, R. A. Cox and D. E. Candeland, *J. Atmos. Chem.*, 1985, **2**, 359-375.
10. B. Laszlo, M. J. Kurylo and R. E. Huie, *J. Phys. Chem.*, 1995, **99**, 11701-11707.
11. A. S. Mahajan, M. Sorribas, J. C. Gómez Martín, S. M. MacDonald, M. Gil, J. M. C. Plane and A. Saiz-Lopez, *Atmos. Chem. Phys.*, 2010, **10**, 27227-27253.
12. C. D. O'Dowd, K. Hameri, J. Makela, M. Vakeva, P. Aalto, G. de Leeuw, G. J. Kunz, E. Becker, H. C. Hansson, A. G. Allen, R. M. Harrison, H. Berresheim, M. Geever, S. G. Jennings and M. Kulmala, *J. Geophys. Res. [Atmos.]*, 2002, **107**, 8107.
13. G. McFiggans, C. S. E. Bale, S. M. Ball, J. M. Beames, W. J. Bloss, L. J. Carpenter, J. Dorsey, R. Dunk, M. J. Flynn, K. L. Furneaux, M. W. Gallagher, D. E. Heard, A. M. Hollingsworth, K. Hornsby, T. Ingham, C. E. Jones, R. L. Jones, L. J. Kramer, J. M. Langridge, C. Leblanc, J. P. LeCrane, J. D. Lee, R. J. Leigh, I. Longley, A. S. Mahajan, P. S. Monks, H. Oetjen, A. J. Orr-Ewing, J. M. C. Plane, P. Potin, A. J. L. Shillings, F. Thomas, R. von Glasow, R. Wada, L. K. Whalley and J. D. Whitehead, *Atmos. Chem. Phys.*, 2010, **10**, 2975-2999.
14. W. J. Bloss, D. M. Rowley, R. A. Cox and R. L. Jones, *J. Phys. Chem. A*, 2001, **105**, 7840-7854.
15. J. C. Gómez Martín, P. Spietz and J. P. Burrows, *J. Phys. Chem. A*, 2007, **111**, 306-320.
16. J. C. Gómez Martín and J. M. C. Plane, *Chem. Phys. Lett.*, 2009, **474**, 79-83.
17. S. Pechtl, E. R. Lovejoy, J. B. Burkholder and R. von Glasow, *Atmos. Chem. Phys.*, 2006, **6**, 505-523.
18. J. C. Gómez Martín, S. H. Ashworth, A. S. Mahajan and J. M. C. Plane, *Geophys. Res. Lett.*, 2009, **36**, L09802, doi:09810.01029/02009GL037642.
19. J. B. Burkholder, J. Curtius, A. R. Ravishankara and E. R. Lovejoy, *Atmos. Chem. Phys.*, 2004, **4**, 19-34.
20. J. L. Jimenez, R. Bahreini, D. R. Cocker, III, H. Zhuang, V. Varutbangkul, R. C. Flagan, J. H. Seinfeld, C. D. O'Dowd and T. Hoffmann, *J. Geophys. Res.*, 2003, **108**, 4318.
21. R. W. Saunders and J. M. C. Plane, *Environ. Chem.*, 2005, **2**, 299-303.
22. L. Pirjola, C. O'Dowd, Y. J. Yoon and K. Sellegri, *Environ. Chem.*, 2005, **2**, 271-281.
23. R. W. Saunders, A. S. Mahajan, J. C. Gómez Martín, R. Kumar and J. M. C. Plane, *Z. Phys. Chem.*, 2010, **224**, 1095-1117.
24. G. Daehlie and A. Kjekshus, *Acta Chem. Scand.*, 1964, **18**, 144.
25. K. Selte and A. Kjekshus, *Acta Chem. Scand.*, 1970, **24**, 1912.
26. A. C. Vikis and R. MacFarlane, *J. Phys. Chem.*, 1985, **89**, 812-815.
27. R. W. Saunders and J. M. C. Plane, *J. Aerosol Sci*, 2006, **37**, 1737.
28. A. Wikjord, P. Taylor, D. Torgerson and L. Hachkowski, *Thermochim. Acta*, 1980, **36**, 367-375.

View Article Online
DOI: 10.1039/C3CP51217G

29. H. Fjellvag and A. Kjekshus, *Acta Chem. Scand.*, 1994, **48**, 815-822.
30. M. A. Blitz, A. Goddard, T. Ingham and M. J. Pilling, *Rev. Sci. Instrum.*, 2007, **78**, 034103.
31. O. Gálvez, J. C. Gómez Martín, P. C. Gómez, A. Saiz-Lopez and L. F. Pacios, *Submitted*, 2013.
32. A. H. Cutler, M. J. Antal and M. Jones, *Industrial & Engineering Chemistry Research*, 1988, **27**, 691-697.
33. M. F. R. Mulcahy and M. R. Pethard, *Aust. J. Chem.*, 1963, **16**, 527-543.
34. M. T. Baeza-Romero, M. A. Blitz, A. Goddard and P. W. Seakins, *Int. J. Chem. Kinet.*, 2012, **44**, 532-545.
35. L. A. LaJohn, P. A. Christiansen, R. B. Ross, T. Atashroo and W. C. Ermler, *J. Chem. Phys.*, 1987, **87**, 2812-2824.
36. L. F. Pacios and P. A. Christiansen, *J. Chem. Phys.*, 1985, **82**, 2664-2671.
37. L. F. Pacios and O. J. Gálvez, *J. Chem. Theory Comput.*, 2010, **6**, 1738-1752.
38. L. V. Gurvich, I. V. Veyts and C. B. Alcock, *Thermodynamic Properties of Individual Substances, Fouth Edition*, Hemisphere Pub. Co., New York, 1989.
39. K. S. Dooley, J. N. Geidosch and S. W. North, *Chem. Phys. Lett.*, 2008, **457**, 303-306.
40. S. H. Robertson, D. R. Glowacki, C.-H. Liang, C. Morley, R. Shannon, M. Blitz and M. J. Pilling, MESMER (Master Equation Solver for Multi-Energy Well Reactions), http://sourceforge.net/projects/mesmer.
41. D. R. Glowacki, C.-H. Liang, C. Morley, M. J. Pilling and S. H. Robertson, *J. Phys. Chem. A*, 2012, **116**, 9545-9560.
42. S. H. Robertson, M. J. Pilling, D. L. Baulch and N. J. B. Green, *J. Phys. Chem.*, 1995, **99**, 13452-13460.
43. J. W. Davies, N. J. B. Green and M. J. Pilling, *Chem. Phys. Lett.*, 1986, **126**, 373-379.
44. R. G. Gilbert and S. C. Smith, *Theory of Unimolecular and Recombination Reactions*, Blackwell, Oxford, 1990.
45. D. J. Grant, E. B. Garner, M. H. Matus, M. T. Nguyen, K. A. Peterson, J. S. Francisco and D. A. Dixon, *J. Phys. Chem. A*, 2010, **114**, 4254-4265.
46. K. A. Peterson, *Mol. Phys.*, 2010, **108**, 393- 408
47. T. J. Dillon, M. E. Tucceri and J. N. Crowley, *PCCP*, 2006, **8**, 5185-5198.
48. L. Shampine and M. Reichelt, *SIAM Journal on Scientific Computing*, 1997, **18**, 1-22.
49. J. W. Gallagher, C. E. Brion, J. A. R. Samson and P. W. Langhoff, *J. Phys. Chem. Ref. Data*, 1988, **17**, 9-145.
50. C. A. Taatjes, N. Hansen, D. L. Osborn, K. Kohse-Hoinghaus, T. A. Cool and P. R. Westmoreland, *PCCP*, 2008, **10**, 20-34.
51. N. Kaltsoyannis and J. M. C. Plane, *PCCP*, 2008, **10**, 1723-1733.
52. M. W. Chase, *J. Phys. Chem. Ref. Data*, 1996, **25**, 1297-1340.
53. Z. Zhang, P. S. Monks, L. J. Stief, J. F. Liebman, R. E. Huie, S.-C. Kuo and R. B. Klemm, *J. Phys. Chem.*, 1996, **100**, 63-68.
54. S. Y. Lee, *J. Phys. Chem. A*, 2004, **108**, 10754-10761.
55. M. E. Tucceri, T. J. Dillon and J. N. Crowley, *PCCP*, 2005, **7**, 1657-1663.